Supplementary Material – The impact of binary stars on the dust and metal evolution of galaxies

Robert M. Yates[1,2]⋆, David Hendriks[2], Aswin P. Vijayan[3,4], Robert G. Izzard[2], Peter A. Thomas[5], and Payel Das[2]
[1]Centre for Astrophysics Research, University of Hertfordshire, Hatfield, AL10 9AB, UK
[2]Department of Physics, University of Surrey, Stag Hill, Guildford, GU2 7XH, UK
[3]Cosmic Dawn Center (DAWN)
[4]DTU-Space, Technical University of Denmark, Elektrovej 327, DK-2800 Kgs. Lyngby, Denmark
[5]Astronomy Centre, University of Sussex, Falmer, Brighton BN1 9QH, UK

Accepted XXX. Received YYY; in original form ZZZ

ABSTRACT

In this supplementary material, we provide additional figures and information related to the main journal paper entitled "The impact of binary stars on the dust and metal evolution of galaxies". This includes (a) visualisations of the chemical yields ejected by stellar populations generated by the BINARY_C code at all six initial metallicities, (b) dust timescale scaling relations for galaxies at redshifts $z = 0$, 1, and 3, and (c) radial profiles for an extended range of galaxy properties at $z = 0$. A list of the key parameter values used when generating our BINARY_C stellar populations is also provided.

Key words: methods: analytical – methods: numerical – stars: binaries – galaxies: abundances – galaxies: evolution.

S1 INTRODUCTION

The impact of stellar evolution on the overall chemical composition of galaxies changes with time. This is because of (a) delayed enrichment and energy deposition from some stars and supernovae (SNe), and (b) the dependence of stellar lifetimes, nucleosynthesis products, and end states on metallicity, which itself changes as galaxies evolve. Therefore, it is important to consider different cosmic epochs and metallicities when analysing galaxy chemical evolution (GCE).

To this end, we here provide additional information and figures to supplement the analysis of the L-GALAXIES semi-analytic galaxy evolution simulation (Springel et al. 2005; Guo et al. 2011; Henriques et al. 2015, 2020) presented in the main paper. The new L-GALAXIES is built on the 'modified model' presented by Yates et al. (2021), with additional implementations for (a) binary stellar evolution (BSE) using the BINARY_C[1] code (Izzard et al. 2006, 2009, 2018; Izzard & Jermyn 2022) and (b) dust production and destruction based on the model from Vijayan et al. (2019). Two versions of this new L-GALAXIES simulation are considered; one including binary+single stars (hereafter, MM+BINARY_C) and one including single stars only (hereafter, MM+singleStars). For more information on the new physics models, see the main paper. For more general information on the underlying L-GALAXIES simulation, see Henriques et al. (2020), Yates et al. (2021), and the Model Description[2].

In Section S2, we provide a list of the key parameter values assumed when generating our mixed and single-star-only stellar populations from BINARY_C. We also present figures comparing the chemical yields from BINARY_C to those from the single-star-only model used previously in L-GALAXIES (see Yates et al. 2013, hereafter Y13). In Section S3, we present the key dust timescales defining our dust model at $z \sim 0$, 1, and 3, as well as the relation between H_2 surface density and the grain growth accretion timescale at those redshifts. Finally, in Section S4 we provide radial profiles for an additional five galaxy properties, to supplement those provided in section 5.4 of the main paper. Throughout, we take a Hubble parameter of $h \equiv H_0/100 = 0.673$, log to the base 10, and distances in co-moving units.

S2 BINARY STELLAR EVOLUTION (BSE) MODEL

S2.1 BINARY_C parameters

Here, we provide a list of the key parameter values assumed in BINARY_C when generating the stellar populations (also known as 'ensembles') used as inputs into L-GALAXIES (see section 3 of the main paper). These parameters define the key physics assumed and are separated into ten sub-categories accordingly. A full list of parameter values can be found in the metadata provided in the ensemble files themselves. These are available online (in JSON format) along with the full L-GALAXIES source code on the L-GALAXIES GitHub repository[3]. For a full description of all the BINARY_C parameters, see the BINARY_C-PYTHON website[4].

⋆ E-mail: r.yates3@herts.ac.uk
[1] https://gitlab.com/binary_c
[2] https://lgalaxiespublicrelease.github.io/Hen20_doc.pdf
[3] lgalaxiespublicrelease.github.io/
[4] https://binary_c.gitlab.io/binary_c-python/

- Build parameters:

  - `version: 2.2.1`
  - `build: Mar 16 2022 21:48:53`
  - `binary_c_python_version: 0.9.4`

- Ensemble parameters:

  - `ensemble_codes: [6d984eac, dab8bea4, 3083cc1f, 47cd834d, d723bdf4, a28ea3be]`
  - `ensemble_metallicities: [0.0001, 0.001, 0.004, 0.008, 0.01, 0.03]`

- Timestep parameters:

  - `ensemble_logdt: 0.1` [log(Myr)]
  - `ensemble_startlogtime: 0.1` [log(Myr)]
  - `max_evolution_time: 15000` [Myr]

- Population parameters:

  - `mmin: 0.08` [$M_{\odot}$]
  - `mmax: 80.0` [$M_{\odot}$]
  - `IMF_distribution: kroupa2001` [Kroupa (2001)]
  - `binaries: True`
  - `dists: Moe` [Moe & Di Stefano (2017)]
  - `separation: 0`

- CE parameters:

  - `comenv_prescription: 0` [Hurley et al. (2002)]
  - `alpha_ce: 1.0`
  - `lambda_ce: 0.5`
  - `post_ce_adaptive_menv: False`
  - `lambda_ionisation: 0.5`

- AGB parameters:

  - `eagbwind: 0` [Hurley et al. (2002)]
  - `tpagbwind: 0` [Karakas et al. (2002)]
  - `postagbwind: 0`
  - `lambda_min: 0` [Izzard et al. (2004)]
  - `delta_mcmin: 0` [Izzard et al. (2004)]

- SN-Ia parameters:

  - `type_Ia_MCh_supernova_algorithm: 0` [DD2 Iwamoto et al. (1999)]
  - `mass_accretion_for_eld: 0.15` [$M_{\odot}$]
  - `WDWD_merger_algorithm: 0` [Hurley et al. (2002)]

- SN-II parameters:

  - `monte_carlo_kicks: True`
  - `sn_kick_dispersion_II: 190` [km/s]
  - `sn_kick_distribution_II: 1` [Maxwellian]

- Black hole parameters:

  - `BH_prescription: 0` [Hurley et al. (2002)]
  - `sn_kick_dispersion_BH_BH: 0` [fixed]
  - `sn_kick_dispersion_BH_NS: 0` [fixed]
  - `sn_kick_dispersion_NS_NS: 0` [fixed]

- Other stellar evolution parameters:

  - `gbwind: 0` [Hurley et al. (2002)]
  - `RLOF_method: 0` [Hurley et al. (2002)]
  - `use_periastron_Roche_radius: False`
  - `no_thermohaline_mixing: False`
  - `E2_prescription: 0` [Hurley et al. (2002)]
  - `CRAP_parameter: 0`
  - `rotationally_enhanced_mass_loss: 0` [none]
  - `tidal_strength_factor: 1`
  - `nucsyn_solver: 0` [Kaps-Rentrop scheme]

S2.2 Stellar yields

Fig. S1 shows the metal ejection rate for mixed (i.e. binary+single) stellar populations generated by BINARY_C at all six initial metallicities considered, [$Z = 0.0001, 0.001, 0.004, 0.008, 0.01, 0.03$]. As described in the main paper, the metal ejection rate from stellar winds (blue) is strongly dependent on metallicity, due to the increased opacity driving increased radiation pressure on the outer layers. The strength of red giant branch (GB) and Wolf-Rayet (WR) winds also increases with metallicity due to this effect. The peak of metal ejection also shifts from $\sim$ 5 Myr at $Z = 0.0001$ to $\sim$ 10 Myr at $Z = 0.03$, due to a decrease in prompt SNe-Ibc with metallicity.

Figs. S2 & S3 show the total mass ejection rates (top row), total metal ejection rates (middle row), and SN rates (bottom row) at different initial metallicities (columns) for ejection sources categorised into 'Wind' (blue), 'SN-II' (orange), and 'SN-Ia' (green) groups, as defined in section 3.3 of the main paper. For this figure, a constant star-formation rate (SFR) of $\psi = 1$ $M_{\odot}$/yr is assumed and three different model set-ups are considered: (a) the mixed stellar populations from BINARY_C (solid lines), (b) single-star-only stellar populations from BINARY_C (dashed lines), and (c) the single-star-only model including SNe-Ia from Y13 (dotted lines).

For the Wind group, we can see a significant increase in ejection rates at early times ($t \lesssim 60$ Myr) when binary stars are included. This is due to the inclusion of common envelope (CE) ejection. At later times, the BINARY_C set-ups under-predict the total amount of metal ejected by AGB stars at low metallicities ($Z \leq 0.004$) and over-estimate this at high metalicities ($Z \geq 0.008$) compared to the Y13 set-up. This is due predominantly to the different yield sets used, as discussed below.

For the SN-II group, the Y13 model predicts an earlier onset of ejection at all metallicities. This is because of the higher upper-mass limit for SNe-II progenitors of 120 $M_{\odot}$ in that set-up, comapred to 80 $M_{\odot}$ for the BINARY_C set-ups. The total mass ejected by the SN-II group is roughly the same in all three set-ups, despite slightly lower overall SN-II rates in the BINARY_C models. This leads to a similar SN feedback strength in L-GALAXIES either with and without binary stars. However, the total *metal* mass ejected is higher in the BINARY_C set-ups, particularly at low metallicities, due to lower predicted remnant masses. For more details, see section 5.1 of the main paper.

For the SN-Ia group, there is a clear under-prediction of the total mass and metal yield from the mixed BINARY_C set-up compared to Y13. This is also reflected in the much lower SN-Ia rates, as discussed in section 3.1.4 of the main paper.

Finally, Figs. S4 & S5 show elemental mass ejection rates for the 11 chemical elements considered (rows) at six different metallicities (columns), assuming a single burst of star formation. At low metallicities (i.e. $Z \leq 0.001$), the overall carbon ejection in the BINARY_C set-ups is only $\sim$ 62 per cent of that in the Y13 set-up, due predominantly to lower carbon yields from AGB stars, as described in the main paper. By $Z = 0.004$, the overall carbon yields become roughly the same between the set-ups, as enhanced carbon ejection from the SNII group in BINARY_C becomes more significant, balancing the deficit from AGB stars.

Conversely, the total nitrogen yield is boosted to up to $\sim$ 137 per cent of the Y13 value in the mixed BINARY_C model at low

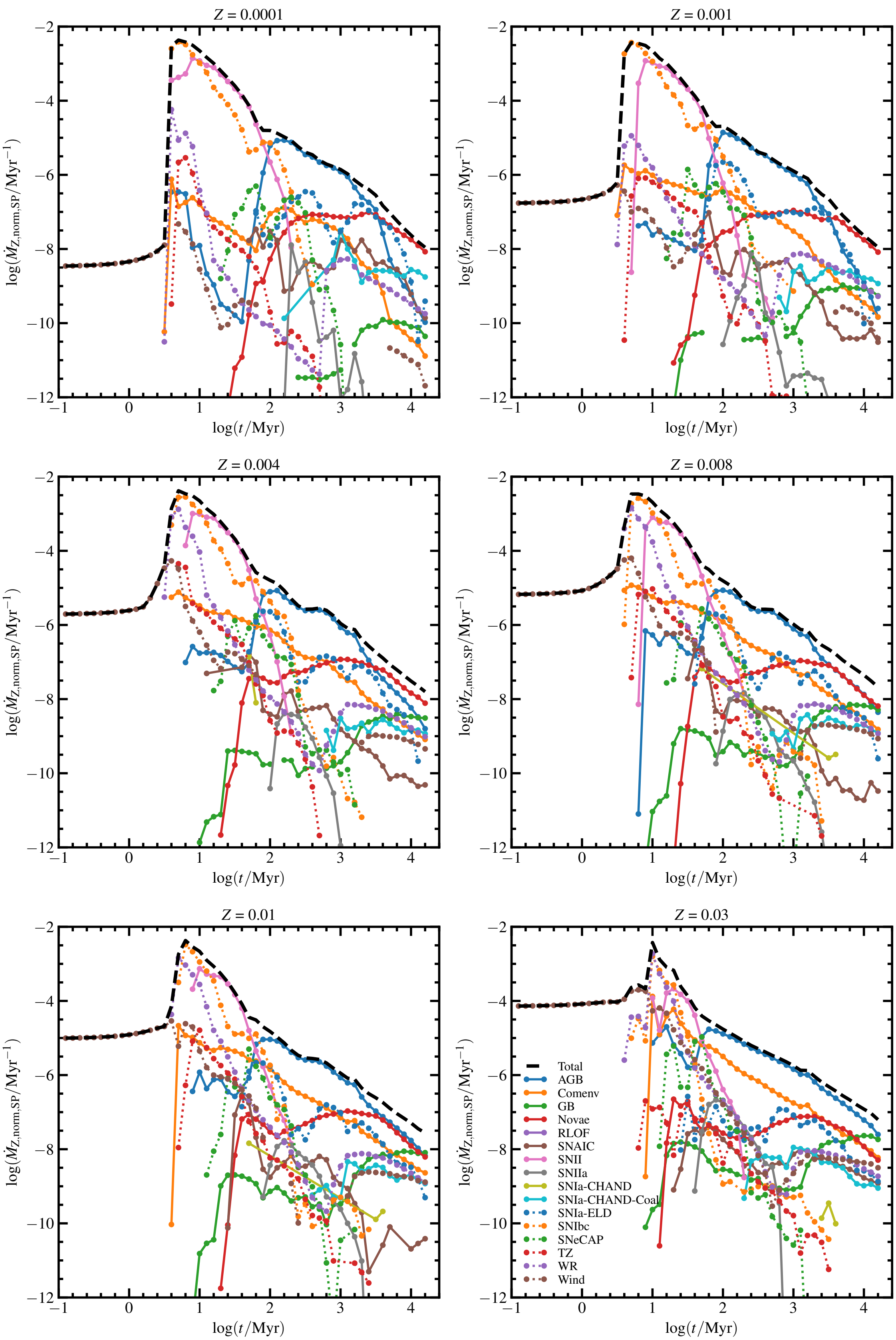

Figure S1. The normalised metal ejection rate ($\dot{M}_{\mathrm{Z,norm}} = \mathrm{d}M_{\mathrm{Z}}/\mathrm{d}t\ 1/\mathrm{M}_{\odot}$), for a BINARY_C stellar population including binary + single stars for six different metallicities $[Z = 0.0001, 0.001, 0.004, 0.008, 0.01, 0.03]$. The 16 different ejection processes considered in BINARY_C are shown, with the total rate from all ejection processes shown as the black dashed line.

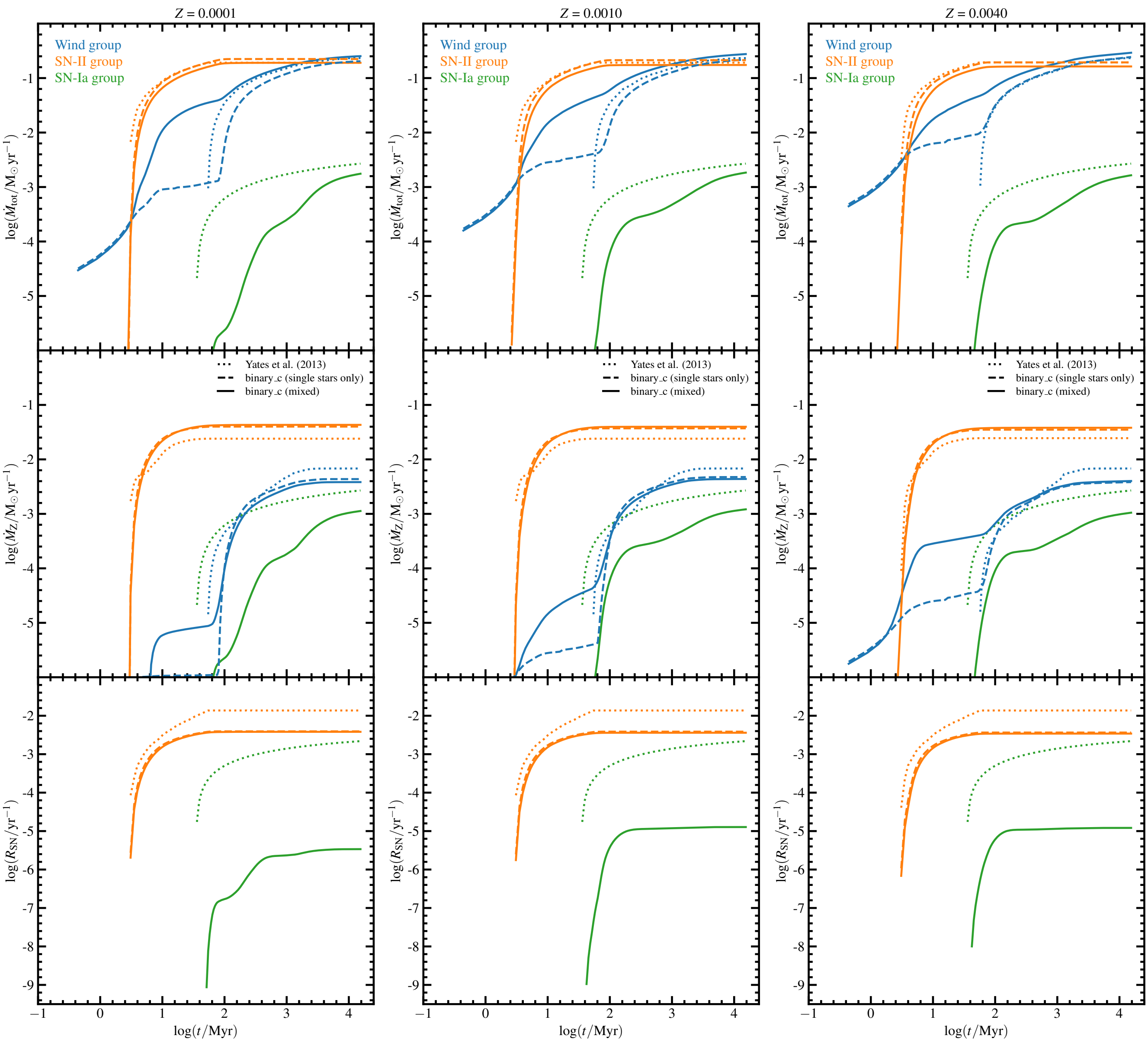

Figure S2. Total mass ejection rates (top row), metal mass ejection rates (middle row), and SN rates (bottom row) for AGB group (blue), SNe-II group (orange), and SN-Ia group (green) ejecta (as defined in section 3.3 of the main paper) assuming a constant SFR of ψ = 1 M$_\odot$/yr for three different metallicities [$Z = 0.0001, 0.001, 0.004$] (columns). Dotted lines denote the single-star-only set-up from previous L-Galaxies versions, dashed lines denote the single-star-only set-up from binary_c, and solid lines denote the binary+single set-up from binary_c.

metallicities, due to enhanced ^{14}N ejection from CE, novae, AGB stars, and SNe-Ia. The neon ejection rate is also significantly larger in the binary_c set-ups compared to Y13. Total neon ejection per stellar population is up to ~ 329 per cent greater in binary_c at low metallicities, dropping to ~ 204 per cent of that from the Y13 set-up at Z = 0.01. This is predominantly due to enhanced yields from the SN-II group, similar to that seen for oxygen (see section 5.1 of the main paper).

Interestingly, iron production in the mixed binary_c set-up is actually larger than in the Y13 set-up at very low metallicities (Z = 0.0001), despite a significant under-prediction of the SNe-Ia rate. This is due to enhanced iron yields from SNe-Ibc. However, the overall iron ejection rate quickly drops as metallicity increases, reaching just ~ 52 per cent of that from the Y13 set-up by Z = 0.008.

S3 DUST MODEL

Fig. S6 shows the dependence of the dust production and destruction timescales in our new L-Galaxies dust model on gas-phase oxygen abundance or galaxy stellar mass at three distinct redshifts, z = 0.0, 1.04, and 3.11. This allows us to analyse how their impact on net dust production changes over time.

The first column of the top three rows of Fig. S6 shows how grain growth accretion timescales, $\tau_{\rm acc}$, are typically much longer at z ~ 3 than the present day. This is due to lower dust masses at higher redshifts in most systems, which are reflected in their lower gas-phase metallicities. As galaxies increase in metallicity and dust mass, $\tau_{\rm acc}$ slowly decreases until there is enough dust present in molecular clouds for grain growth to become highly efficient. This causes a sharp drop in $\tau_{\rm acc}$, followed by a more steady decrease at

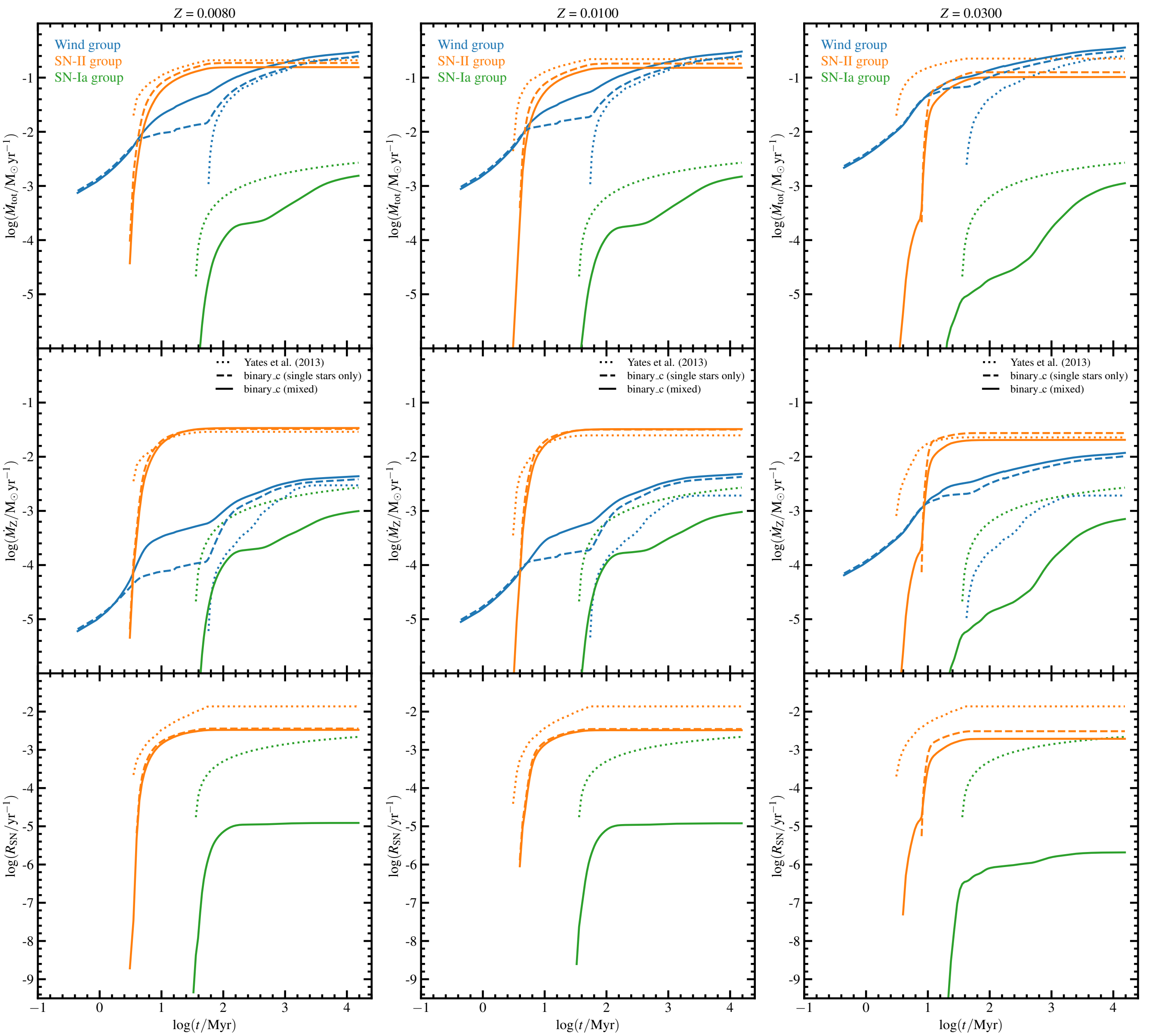

Figure S3. Same as Fig. S2, but for three different metallicities $[Z = 0.008, 0.01, 0.03]$.

higher metallicities once grain growth becomes limited by the dust destruction rate (i.e. becomes saturated).

The second column of the top three rows of Fig. S6 shows how the local SN shock destruction rate in the interstellar medium (ISM), $\tau_{\rm shock}$, becomes longer than a Hubble time in an increasing number of galaxies from $z \sim 3$ to 0. These regions are predominantly in early-type galaxies, which have had their star formation shut down via gas exhaustion from a merger-induced starburst followed by suppression of gas cooling by active galactic nucleus (AGN) feedback. This increase in galaxies with very long $\tau_{\rm shock}$ therefore reflects the build-up of the galaxy 'red sequence' over cosmic time. There is also typically longer $\tau_{\rm shock}$ in MM+BINARY_C than MM+singleStars at all redshifts, due to lower overall SN rates.

The third and fourth columns of the top three rows illustrate how sputtering timescales in the circumgalactic medium (CGM) and ejecta reservoir surrounding galaxies, $\tau_{\rm sput,CGM}$ and $\tau_{\rm sput,Ejecta}$, slowly increase at fixed stellar mass from $z \sim 3$ to 0. This is due to the decrease in the hot gas mass around galaxies with $\log(M_*/\,{\rm M}_\odot) \lesssim 10.0$ over cosmic time.

The bottom row of Fig. S6 shows the dependence of $\tau_{\rm acc}$ on H_2 mass surface density, $\Sigma_{\rm H2}$, at $z = 0.0$, 1.04, and 3.11. This can be compared to similar plots for the dust models in other cosmological simulations (e.g. Popping et al. 2017). We find that our grain growth formalism returns shorter $\tau_{\rm acc}$ in low- to intermediate-density environments at late times, but marginally longer $\tau_{\rm acc}$ in these environments at early times. This is due to the stronger sensitivity of $\tau_{\rm acc}$ to dust mass in our model.

S4 RADIAL PROFILES

Fig. S7 shows stacked radial profiles for key properties of star-forming disc galaxies at $z = 0.0$, separated into three stellar mass bins, from the MM+BINARY_C (blue) and MM+singleStars (red) versions of L-

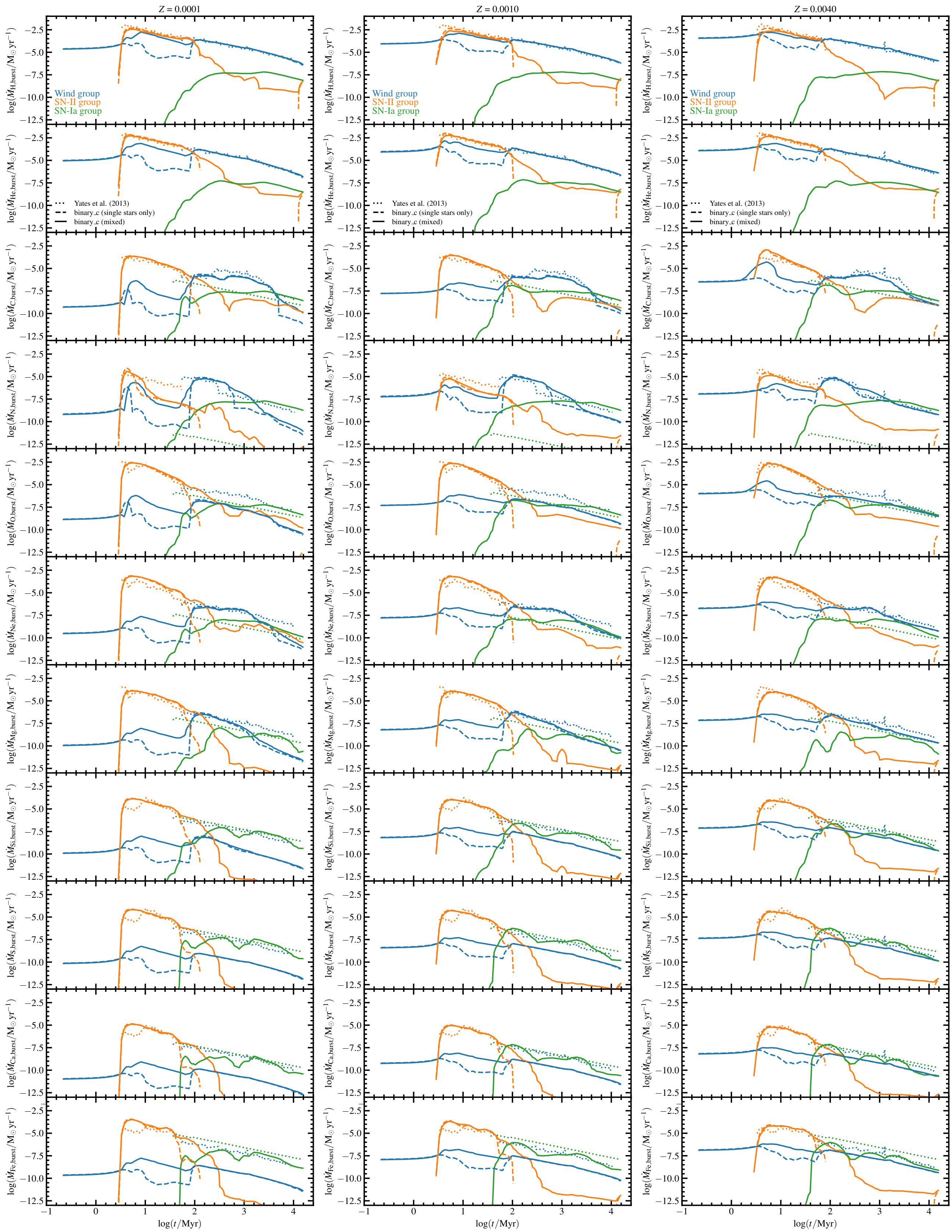

Figure S4. Mass ejection rates from a single $1\,\mathrm{M}_{\odot}/\mathrm{yr}$ burst of star formation for 11 chemical elements (rows) at three different metallicities [$Z = 0.0001, 0.001, 0.004$] (columns). Dotted lines denote the single-star-only set-up from previous L-Galaxies versions, dashed lines denote the single-star-only set-up from binary_c, and solid lines denote the binary+single set-up from binary_c.

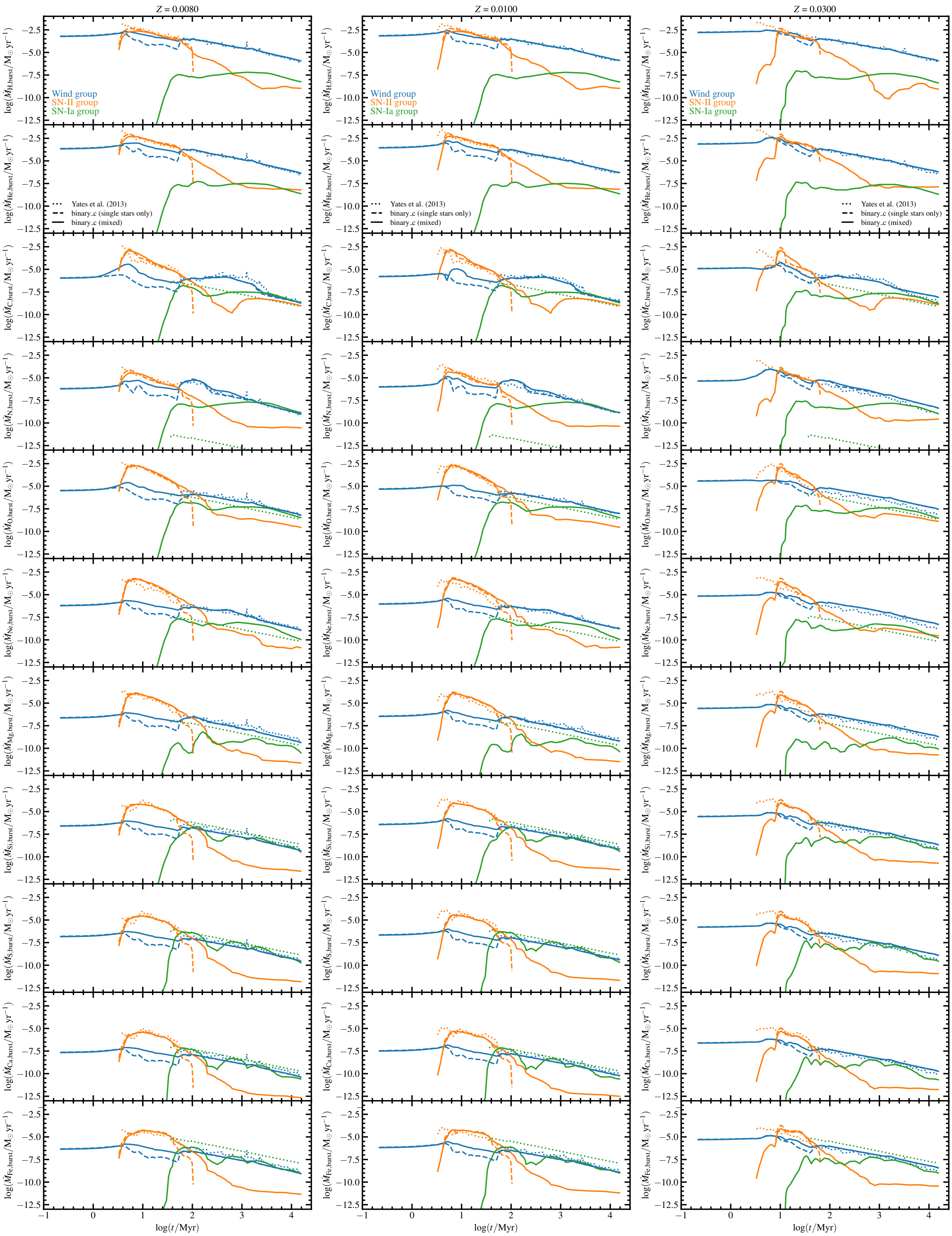

Figure S5. Same as Fig. S4, but at three different metallicities $[Z = 0.008, 0.01, 0.03]$.

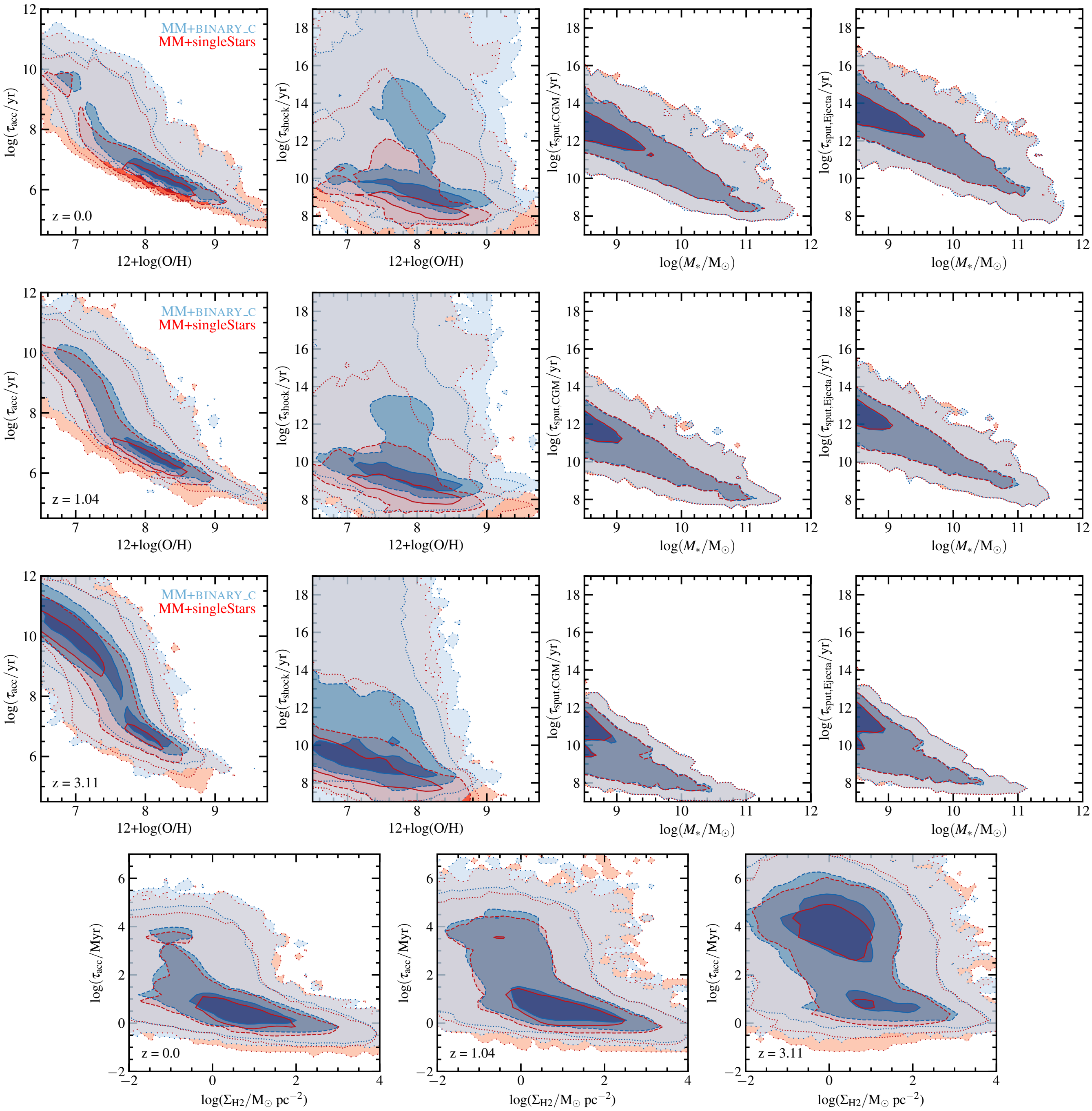

Figure S6. Various dust timescales for the MM+BINARY_C (blue) and MM+singleStars (red) versions of L-GALAXIES run on MILLENNIUM and MILLENNIUM-II combined, considering only "resolved" systems above $\log(M_*/\mathrm{M}_\odot) = 8.0$ from MILLENNIUM and $\log(M_*/\mathrm{M}_\odot) = 7.0$ from MILLENNIUM-II. Contours represent the 1-4 σ spread in the distributions. *Top row:* Dust accretion timescale for grain growth in molecular clouds as a function of ISM oxygen abundance for individual radial rings at $z = 0.0$ (left). Dust destruction timescale for SN shocks in the ISM versus ISM oxygen abundance for individual rings (centre left). Dust destruction timescale for thermal sputtering in the CGM as a function of galaxy stellar mass (centre right). Dust destruction timescale for thermal sputtering in the Ejecta phase as a function of galaxy stellar mass (right). *Second row:* Same as top row, but at $z = 1.04$. *Third row:* Same as top row, but at $z = 3.11$. *Fourth row:* Dust accretion timescale as a function of H_2 surface density for individual radial rings at $z = 0.0$ (left), $z = 1.04$ (centre), and $z = 3.11$ (right).

GALAXIES. These profiles supplement those shown in fig. 9 of the main paper.

The top row of Fig. S7 shows the total metallicity profile for disc stars, $Z_{*,\mathrm{disc}}$, normalised to the solar photospheric value of $Z_\odot = 0.0134$ from Asplund et al. (2009). As for the gas-phase oxygen abundance profiles shown in the main paper, stellar metallicities are slightly higher at large radii in MM+BINARY_C compared to MM+singleStars, leading to slightly flatter profiles. This is due to higher α-element yields from SNe-II at low metallicities in the BINARY_C set-up. However, the relative normalisation of the $Z_{*,\mathrm{disc}}$ profile is slightly lower than for the gas-phase metallicity in MM+BINARY_C. This is in part due to the lower carbon yields from

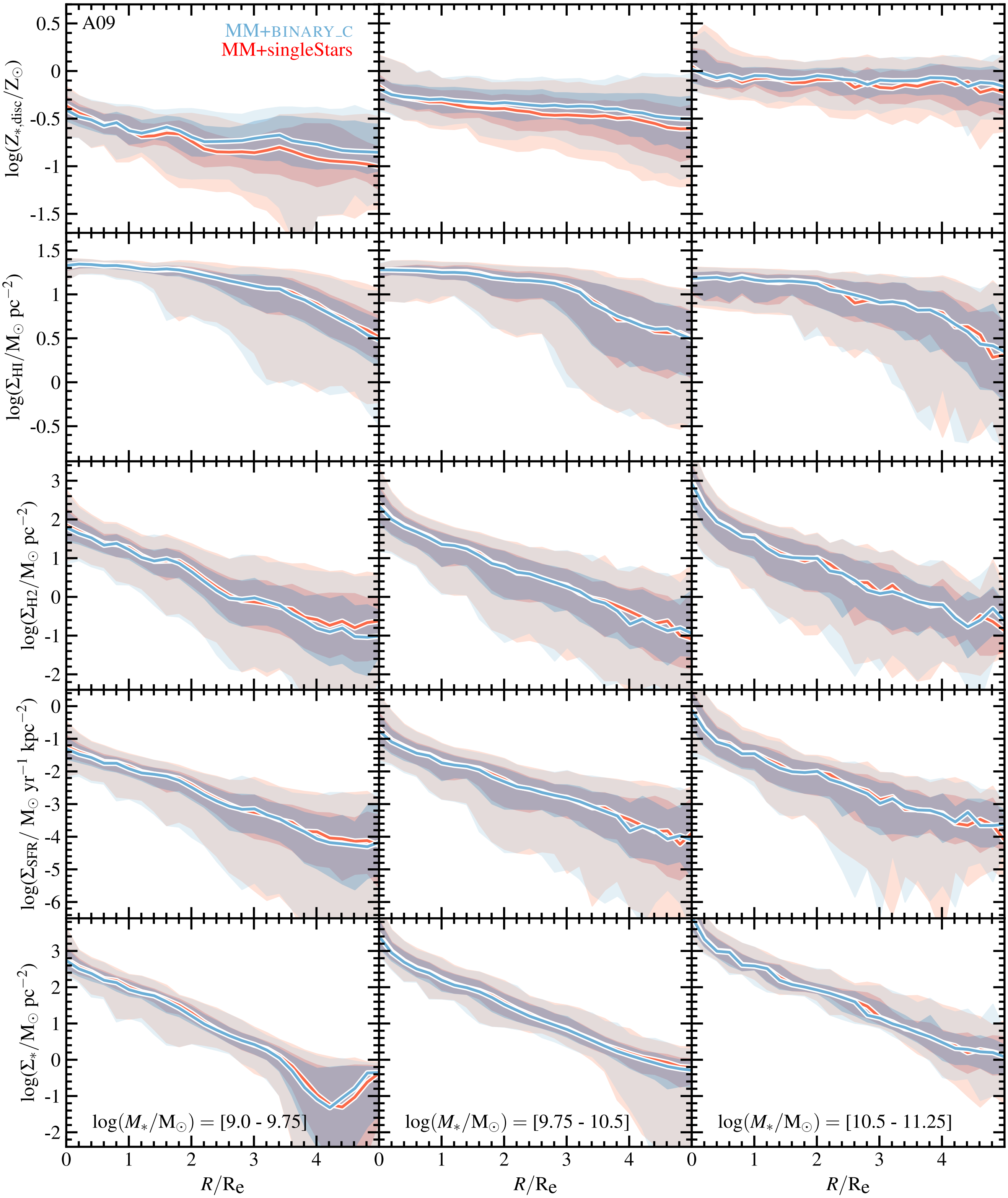

Figure S7. Stacked radial profiles for star-forming galaxies at $z = 0$ from the MM+BINARY_C (blue) and MM+singleStars (red) versions of L-GALAXIES run on MILLENNIUM, separated into three mass bins. *First row:* Overall stellar metallicity in the disc, normalised to the solar photospheric value of $Z_{\odot} \equiv M_{\mathrm{Z},\odot}/M_{\mathrm{b},\odot} = 0.0134$ from Asplund et al. (2009). *Second row:* HI mass surface density. *Third row:* H_2 mass surface density. *Fourth row:* Star-formation rate surface density. *Fifth row:* Stellar mass surface density. In all cases, R_{e} is measured as the half-light radius in the r-band.

low-metallicity AGB stars in BINARY_C (see Section S2), which lead to slightly lower $Z_{*,\mathrm{disc}}$ in the very centres of low-mass galaxies. Unlike oxygen, carbon in the ISM is predominantly locked into dust grains in L-GALAXIES, meaning that its abundance has a smaller effect on the overall gas-phase metallicity than it does on the stellar metallicity.

Lower-mass galaxies spend a larger fraction of their lifetimes at low metallicity, causing the carbon deficit seen in their stars by $z = 0.0$ to be stronger than in more massive systems. Once galaxies reach metallicities of $Z \gtrsim 0.004$, we find carbon abundances become more similar between MM+BINARY_C and MM+singleStars, due to larger carbon yields from SNe-II in BINARY_C.

The remaining rows in Fig. S7 show the stacked profiles for Σ_{HI}, Σ_{H2}, Σ_{SFR}, and Σ_{*}. All these profiles are very similar in MM+BINARY_C and MM+singleStars. As explained in the main paper, this indicates that the non-chemical properties of galaxies are relatively unchanged when switching from a single-star to a mixed formalism, as long as the total mass ejected by massive stars remains the same.

REFERENCES

Asplund M., Grevesse N., Sauval A. J., Scott P., 2009, ARA&A, 47, 481
Guo Q., et al., 2011, MNRAS, 413, 101
Henriques B. M. B., White S. D. M., Thomas P. A., Angulo R., Guo Q., Lemson G., Springel V., Overzier R., 2015, MNRAS, 451, 2663
Henriques B. M. B., Yates R. M., Fu J., Guo Q., Kauffmann G., Srisawat C., Thomas P. A., White S. D. M., 2020, MNRAS, 491, 5795
Hurley J. R., Tout C. A., Pols O. R., 2002, MNRAS, 329, 897
Iwamoto K., Brachwitz F., Nomoto K., Kishimoto N., Umeda H., Hix W. R., Thielemann F.-K., 1999, ApJS, 125, 439
Izzard R. G., Jermyn A. S., 2022, MNRAS,
Izzard R. G., Tout C. A., Karakas A. I., Pols O. R., 2004, MNRAS, 350, 407
Izzard R. G., Dray L. M., Karakas A. I., Lugaro M., Tout C. A., 2006, A&A, 460, 565
Izzard R. G., Glebbeek E., Stancliffe R. J., Pols O. R., 2009, A&A, 508, 1359
Izzard R. G., Preece H., Jofre P., Halabi G. M., Masseron T., Tout C. A., 2018, MNRAS, 473, 2984
Karakas A. I., Lattanzio J. C., Pols O. R., 2002, Publ. Astron. Soc. Australia, 19, 515
Kroupa P., 2001, MNRAS, 322, 231
Moe M., Di Stefano R., 2017, ApJS, 230, 15
Popping G., Somerville R. S., Galametz M., 2017, MNRAS, 471, 3152
Springel V., White S. D. M., Jenkins A., et al., 2005, Nature, 435, 629
Vijayan A. P., Clay S. J., Thomas P. A., Yates R. M., Wilkins S. M., Henriques B. M., 2019, MNRAS, 489, 4072
Yates R. M., Henriques B., Thomas P. A., Kauffmann G., Johansson J., White S. D. M., 2013, MNRAS, 435, 3500
Yates R. M., Henriques B. M. B., Fu J., Kauffmann G., Thomas P. A., Guo Q., White S. D. M., Schady P., 2021, MNRAS, 503, 4474

This paper has been typeset from a TEX/LATEX file prepared by the author.